Journal of Materials Science & Technology 105 (2022) 203–213

Contents lists available at ScienceDirect

Journal of Materials Science & Technology

journal homepage: www.elsevier.com/locate/jmst

Research Article

Impact of gas pressure on particle feature in Fe-based amorphous alloy powders *via* gas atomization: Simulation and experiment

Yutong Shi[a,b], Weiyan Lu[a], Wenhai Sun[a], Suode Zhang[a], Baijun Yang[a], Jianqiang Wang[a,*]

[a] Shenyang National Laboratory for Materials Science, Institute of Metal Research, Chinese Academy of Sciences, Shenyang 110016, China
[b] School of Materials Science and Engineering, University of Science and Technology of China, Shenyang 110016, China

ARTICLE INFO

Article history:
Received 25 January 2021
Revised 25 June 2021
Accepted 29 June 2021
Available online 20 September 2021

Keywords:
Gas atomization
Fe-based amorphous powder
Closed-wake
Gas-melt flow
Break-up
Particle size distribution

ABSTRACT

Gas atomization is now an important production technique for Fe-based amorphous alloy powders used in additive manufacturing, particularly selective laser melting, fabricating large-sized Fe-based bulk metallic glasses. Using the realizable k-ε model and discrete phase model theory, the flow dynamics of the gas phase and gas-melt two-phase flow fields in the close-wake condition were investigated to establish the correlation between high gas pressure and powder particle characteristics. The locations of the recirculation zones and the shapes of Mach disks were analyzed in detail for the type of discrete-jet closed-coupled gas atomization nozzle. In the gas-phase flow field, the vortexes, closed to the Mach disk, are found to be a new deceleration method. In the two-phase flow field, the shape of Mach disk changes from "*S*"-shape to "*Z*"-shape under the impact of the droplet flow. As predicted by the wave model, with the elevation of gas pressure, the size of the particle is found to gradually decrease and its distribution becomes more concentrated. Simulation results were compliant with the Fe-based amorphous alloy powder preparation tests. This study deepens the understanding of the gas pressure impacting particle features *via* gas atomization, and contributes to technological applications.

1. Introduction

Additive manufacturing (AM) is a speedily developing manufacturing technology, which is also known as direct digital manufacturing and 3D printing. Different from the traditional manufacturing technologies (TMT), AM is a procedure of adding feedstock materials (powers, wires, etc.) to manufacture the final products layer by layer [1–7]. Thus, it has the potential to produce more complicated parts-on-demand with a fast manufacturing rate, low energy consumption, and capitalized cost [8,9]. In addition, the products manufactured by AM are better than those produced by TMT in some diverse factors, such as the complex geometries, the relatively low number of parts, and the shorter timescales. However, the quality is significantly influenced by the features of the raw materials [4,10], such as the powder size distribution, composition, shape, and surface morphology [2,11,12]. Therefore, an assessment of the manufacturing routes of alloy powders and their respective performances during the AM processes is of utmost importance.

In general, the characteristics of the particles are closely related to the production technique. Techniques that are frequently utilized include gas atomization [13], water atomization (WA) [14], plasma atomization (PA) [3] and others. A few atomization techniques produce powders with irregular appearances (*e.g.*, WA), while others may not be economically friendly (*e.g.*, PA) [8]. Gas atomization manufacture in powder metallurgy has been elucidated as the fragmentation of molten metal into a large number of liquid metal droplets by the impingement of gas flow with high speed [15]. The molten alloy droplets subsequently will go through spheroidization, cooling and solidification into alloy particles, typically ranging from several to hundreds of micrometers in diameter [16]. The high cooling rate (10^4–10^6 K/s) and deep undercooling of gas atomization make it possible to produce powders with reduced segregation and desirable microstructure [7]. In addition, the amorphous structure alloy powders or metallic glass (MG) powders, which exhibit better characteristics such as great tensile strength, hardness, wear resistance, and corrosion resistance [17], can also be obtained under the above cooling condition. Because of their superior properties, a number of MG powders have been investigated and synthesized by ambient and hot gas atomization at various melt flow rates [18]. However, the detailed physical behavior during the production of MG powders has not been completely understood. The difficulty mainly stems from the lack of in-depth perception of the gas-metal interactive effect, the disintegration of melt, and distribution of the molten alloy flow within the atomization region.

* Corresponding author.
E-mail address: jqwang@imr.ac.cn (J. Wang).

https://doi.org/10.1016/j.jmst.2021.06.075
1005-0302/

Extensive studies in recent years focused on elucidating the physical process during atomization. Utilizing a computational fluid dynamics (CFD) method, Ting et al. [19,20] calculated the gas flow field of an annular-slit high-pressure gas atomization nozzle and analyzed the stagnation pressure fronts in the open-wake and the closed-wake conditions. It was found that the flow field presented an open-wake situation at low atomization gas pressures and the closed-wake phenomenon occurred when an atomization pressure is as high as 4.82 MPa. Zeoli et al. [12,16,21] computed the fragmentation and solidification behavior throughout the secondary atomization of a molten alloy. They found that, the melt started to disintegrate immediately when hit by the high velocity gas, the large droplets burst into smaller particles and the initial small droplets were atomized to micro-size particles with highly narrow ranges of size distribution throughout the secondary disruption. Li and Fritsching [22] presented a widespread approach to accomplish integral of modeling and simulation for metal powder production. Narrower droplet-size distributions compared to the experimental measurements were obtained by the three droplet breakup models, Taylor analogy breakup (TAB) model, Enhanced Taylor analogy breakup (ETAB) model and empirical model. In addition, Thompson et al. [23] made a 3D axi-symmetric simulation of a close-coupled atomizing melt-nozzle. Based upon the two-way coupling of the CFD with the discrete phase model (DPM) and the Euler-Lagrange method, they demonstrated that the eventual diameter distributions of the manufactured metal powders were sensitive to the process parameters. In order to understand the atomization procedure and theory of vacuum induction melting gas atomization accurately, a novel method was supported by the complex of VOF and DPM [24]. A contrast of the SST k-ω model and LES model was researched and Wei et al. utilized the TAB model to compute the particle diameter distribution throughout the secondary breakup. However, it is noteworthy that although the simulation of the open-wake atomization and the transition from the open-wake to the close-wake atomization have been extensively investigated, the characteristic of high-pressure gas atomization in the close-wake condition has been largely neglected.

Herein, to fulfill this gap, we aimed at simulating and understanding the atomization process of Fe-based amorphous alloy powders under different gas pressures ranging from 5 to 8 MPa. The characteristics of the gas flow and gas-melt flow field, in the closed-wake condition, were analyzed using CFD. Further, the unstable breakup model (WAVE model) based on Eular-Lagrange DPM was implemented to calculate the diameters and distributions of glassy powder particles. The calculated simulation outcomes and actual results were compared. Eventually, the influence of gas pressure upon the wake-closure atomization and the disruption of MG powders were elucidated.

2. Numerical modeling

2.1. Gas atomization model and boundary conditions

Since the modeling involved a discrete-jet, close-coupled gas atomization type nozzle, a half of a 2D central cross-section of the orifice with the melt pour tube was selected to represent a rotational symmetry atomization flow field (Fig. 1). The number of discrete-jets for gas is 18, with symmetrical distribution, and the angle is 30 °. The nitrogen (N_2) and molten metal were injected into the atomization chamber respectively through the gas exit and the melt orifice. The computational region was oriented horizontally with the atomizer molten alloy pour and N_2 delivery on the left and the axis of symmetry boundary on the bottom of the atomization flow field, separately. Gambit 2.4.6 was used for meshing. The triangular mesh was employed at the gas inlet, and the quadrilateral mesh at other zone. A part of computational domain including high velocity gradients and close to symmetry boundary had a refined grid during the CFD simulations. The total number of nodes is 97,323, and the number of cells is 158,275. The minimum cell size is 0.1 mm. After meshing, Fluent 19.2 was used for solving, and post processing.

The walls of the computational domain were all hypothesized to keep a sustained temperature of 300 K, while the melt orifice was assumed to be 1500 K. The outlet boundary with ambient pressure was applied at the external domain. Finally, atomization gas pressures of 5–8 MPa were used in the CFD model to initialize the pressure in the gas delivery system, upstream of the discrete jet gas die. The default data of N_2 in Fluent 19.2 were used in this work. As listed in Table 1, the main thermodynamic parameters of Fe-based glassy alloy were from the literature [25–27].

2.2. Modeling the fluid

The 'realizable k-ε model' has been widely applied in the gas atomization calculation. The basic relationships for the 2-D model in the Cartesian tensor rely on the equations:

Mass conservation equation:

$$\frac{\partial \rho}{\partial t} + \frac{\partial}{\partial x_i}(\rho u_i) = 0 \tag{1}$$

Momentum conservation:

$$\frac{\partial}{\partial x_i}(\rho u_i) + \frac{\partial}{\partial x_i}\left(\rho u_i u_j\right) = -\frac{\partial p}{\partial x_i} + \frac{\partial}{\partial x_j}\left(\tau_{ij}\right)_{\text{eff}} + \frac{\partial}{\partial x_j}\left(-\rho\overrightarrow{u'_i u'_j}\right) \tag{2}$$

Energy transport equation:

$$\frac{\partial}{\partial t}(\rho E) + \frac{\partial}{\partial x_i}[u_i(\rho E + p)] = \frac{\partial}{\partial x_j}\left(k_{\text{eff}}\frac{\partial T}{\partial x_j} + u_i\left(\tau_{ij}\right)_{\text{eff}}\right) + S_{\text{h}} \tag{3}$$

$$\left(\tau_{ij}\right)_{\text{eff}} = \mu_{\text{eff}}\left(\frac{\partial u_j}{\partial x_i} + \frac{\partial u_i}{\partial x_j}\right) - \frac{2}{3}\mu_{\text{eff}}\frac{\partial u_i}{\partial x_i}\delta_{ij} \tag{4}$$

where the effective thermal conductivity is given

$$k_{\text{eff}} = k + \frac{c_p \mu}{\sigma_t} \tag{5}$$

In Eqs. (1)–(5), the index i, j indicate the two coordinates of droplet position and velocity components; u_{i} is the fluid phase velocity. μ is the molecular viscosity of the gas. ρ refers to the density of the fluid phase. c_{p} is the specific heat capacity. σ_{t} is the surface tension of the liquid; t is time; p is pressure. The convention will be used here that τ_{ij} denotes a stress in the j direction exerted on a plane perpendicular to the i axis. E is the sum of both internal and kinetic energy; k is the thermal conductivity of the Fe-based alloy melt; T is temperature; S_{h} is the source term. Subscript eff represents the effective value, and subscript t represents the value changes with the temperature, not a constant. δ is Kronecker symbol.

2.3. The discrete particle model

To simulate the melt breaking-up and droplet tracking, a DPM was implemented by the commercial finite volume code Fluent [1]. As for DPM, normally, there are a continuous phase and a discrete phase. The continuous phase takes the space point as the object and calculates its pressure, temperature and density. While the discrete phase tracks the particle and calculates its force, velocity and trajectory. The discrete phase can exchange momentum, heat, and mass with the continuous phase. In this work, N_2 is the continuous phase, and the liquid is the discrete phase. Given the movements of the droplets, their paths were simulated by the integration of a force balance on the respective droplet. There is an equivalence

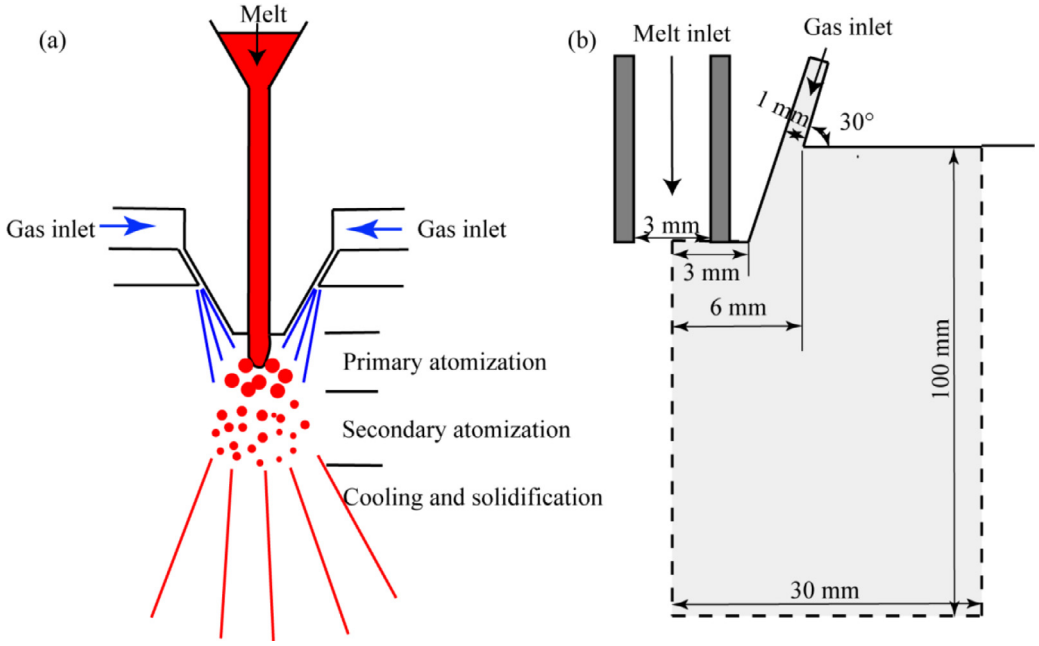

Fig. 1. (a) Schematic drawing of the atomization process, (b) schematic diagram of the atomizer and the computational field (shaded dotted area).

Table 1
The main thermodynamic parameters of Fe-based glassy alloy.

Density (kg/m^3)	Specific heat (J/(K mol)) [25]	Viscosity (Pa s) [26]	Surface tension (N/m) [27]
7820	44.09	5.8×10^{-5}	0.8

between the particle's inertia and the forces which work on it. The following equation is given in the Lagrangian reference frame on the x reference axis [28]

$$\frac{du_d}{dt} = F_D(u - u_d) + \frac{g_x(\rho_d - \rho)}{\rho_d} + F_x \tag{6}$$

where $F_D(u\text{-}u_d)$, the initial term on the right side of the equation, is the drag force among the droplets, and the following term is gravity. Subscript d represents droplets; subscript g represents gas; subscript x represents the x axis. The last term is additional force. The coefficient F_D is expressing as

$$F_D = \frac{18\mu}{\rho_d d_d^2}\frac{C_D \mathrm{Re}}{24} \tag{7}$$

where the droplet Reynolds number (Re) is defined as

$$\mathrm{Re} = \frac{\rho_g d_d |u_{d,i} - u_i|}{\mu_d} \tag{8}$$

In Eqs. (6)–(8), the index i represents the two coordinates of droplet position and velocity components; u_i is the fluid phase velocity, while $u_{d,i}$ shows the velocity of droplet. μ_d is the molecular viscosity of the droplet. ρ_g refers to the density of the gas and ρ_d represents the droplet density. d_d is the droplet diameter. C_D is the drag coefficient and the F_x is a term that allows the incorporation of additional forces [28].

$$F_x = \frac{1}{2}\frac{\rho}{\rho_d}\frac{d}{dt}(u - u_p) + \frac{\rho}{\rho_d}u_p\frac{\partial u}{\partial x} \tag{9}$$

On the right side, the initial term is a "virtual mass" force that accounts for the acceleration of the fluid surrounding the particle and the second term is a pressure gradient that is due to the "local" pressure gradient in the fluid surrounding the particle. The virtual mass becomes important when $\rho > \rho_d$. Obviously, the surrounding gas density is less than the droplet density in this calculation, therefore, the initial term can be ignored.

The wave breakup model, according to Reitz [29], is appropriate for great Weber-number gas flows (We > 100), which insists that the collapse of the droplets is produced by the relative velocity between the gas and liquid phases. This model hypothesizes that the fastest-growing Kelvin-Helmholtz instability determines the time of disintegration and the newly-formed droplet diameter. The wavelength and growth rate of this instability are applied to calculate details of the resulting droplets. In the wave model, disruption of large droplets is simulated by supposing that the radii of the resulting particles are proportional to the wavelength of the fastest-growing unstable surface wave on the initial particles. This relationship can be described with the following equation,

$$r = 9.02B_0 a\frac{\left(1 + 0.45\mathrm{Oh}^{0.5}\right)\left(1 + 0.4\mathrm{Ta}^{0.7}\right)}{\left(1 + 0.87We_2^{1.67}\right)^{0.6}} \tag{10}$$

where B_0 is a model constant set equal to 0.61 according to the work of Reitz, and a is the radius of the liquid jet. $\mathrm{Oh} = \sqrt{\mathrm{We}_1}/\mathrm{Re}_1$ is defined as the Ohnesorge number and $\mathrm{Ta} = \mathrm{Oh}\sqrt{\mathrm{We}_2}$ refers to the Taylor number. Besides, the Weber numbers, which are defined respectively as $\mathrm{We}_1 = \rho_p U^2 a/\sigma_t$ and $\mathrm{We}_2 = \rho_g U^2 a/\sigma_t$, and $\mathrm{Re}_1 = U^2 a/\nu_1$ is the Reynolds number. ν_1 is the liquid kinematic viscosity. The symbol U is for the relative velocity between gas and melt.

3. Experimental procedure

The material applied in this study was $Fe_{50}Cr_{18}Mo_{7.5}Ni_{3.5}P_{12}B_3C_{3.5}Si_{2.5}$ (at.%) alloy. This alloy with the above metal and nonmetallic composition was cast by induction-

melting pure elements (Fe: 99.7, Cr: 99.9, Mo: 98.5, Ni: 99.9, FeB: 99% (22.06 wt.% boron), FeP (21.20 wt.% phosphorous), C: (99.9%), Si: (99.9%) under a high-purity N_2 atmosphere. The amorphous powders were prepared by high-purity N_2 atomization at different atomization pressures of 5–8 MPa and the highest temperature was about 1500 K using a close-coupled discrete-jet nozzle. The internal diameter of the melt pour tube was 3 mm. The batch size is about 20 kg, and the mass flow rate of melt is about 0.067 kg/s. As for the mass flow rate of gas, it depends on the gas pressure, about 0.032–0.046 kg/s. So the gas-to-melt mass flow rate ratio ranges from 0.48 to 0.69. The atomized glassy powders were sieved and separated into different size ranges. The measurements of the particle size distributions were made with a laser diffraction particle size analyzer. The microstructure of the powders was characterized by a Supra 55 scanning electron microscope (SEM). X-ray diffraction (XRD) analysis of the powders was examined by a Rigaku D/max 2400 diffractometer with monochromated Cu K_α radiation ($\lambda = 0.1542$ nm).

4. Results

4.1. Simulation of gas flow field

The simulation began with the computation of N_2 flow before the molten metal was poured. Profiles under the gas pressures of 5–8 MPa are illustrated in Fig. 2(a–d), respectively. At the gas pressure of 5 MPa case in Fig. 2(a), the gas flow expands through internal shocks and recompression shocks hitting the atmosphere inside the atomization chamber. At the corner of the melt tube, the gas flow separates and part of it forms a vortical recirculation zone. This zone is located next to the bottom of the melt tube and delineated by the sonic line. In the recirculation zone, there are upstream and downstream gas flows, with a turbulent layer in the middle. The gas flow along the central axis is observed to move toward the melt orifice and shifts outward radially close to the melt tube. Encountering the turbulent layer, the gas flow is pushed outward and flows downstream. It should be noted that the end of the primary circulation zone is a single stagnation point, where the velocity of gas flow is zero in the centerline. Downstream this point, the gas flow accelerates in the forward direction, and reaches supersonic speed. In this case, the internal shock suddenly collapses to a smaller size, forming a “bowed” Mach disk. Further, the second recirculation zone appears at the downstream of the Mach disk. Obviously, inside this zone, there are two other stagnation points and a diminutive subsonic region close to the Mach disk. After the third stagnation point, the velocity re-accelerates followed by deceleration throughout a variety of Prandtl-Meyer waves in the streamwise direction along the central axis.

When the gas pressure increases to 6 MPa, both the second and the third stagnation points move downstream from the melt orifice. It is noted that the second recirculation zone is lengthened, forming an hourglass-like contour as a result of a recompression shock that enhances strength (Fig. 2(b)). As the atomization gas pressure increases to 7 MPa (Fig. 2(c)), a new small Mach disk appears and cuts off the enlarged hourglass-like second recirculation zone. Accordingly, the second recirculation zone becomes shorter and the third recirculation zone appears. At a pressure of 8 MPa, the primary and second recirculation zones remain stable, while the third recirculation zone becomes lengthened (Fig. 2(d)).

The velocity profiles along the axis of symmetry starting from the melt orifice position at gas pressures ranging from 5 to 8 MPa are shown in Fig. 3. Obviously, with the increase of gas pressure, the magnitudes of velocities and the locations of stagnation fronts remain the same in primary recirculation zones, reflecting similar features occurring in this zone. All the primary stagnation fronts are located at about 1 nozzle diameter length (NDL) (blue arrows).

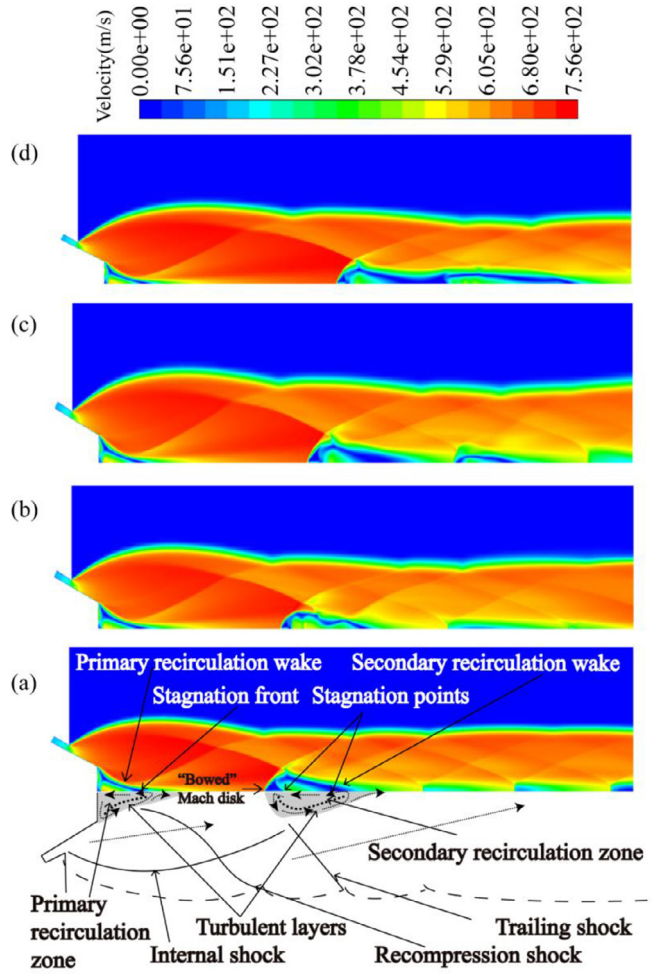

Fig. 2. CFD model of the high-pressure gas atomization nozzle at gas pressures ranging from 5 to 8 MPa in the closed-wake condition. The velocity magnitude increases with decreasing shades of darkness in the CFD figures. (a) The primary and the second recirculation zone at 5 MPa; (b) the primary and the enlarged second recirculation zone at 6 MPa; (c) the primary, the second and third recirculation zone at 7 MPa; (d) the primary, the second the enlarged third recirculation zone at 8 MPa.

After crossing the stagnation front, the velocity of gas increases along the axis and the velocity is up to the maximum value when it approaches the Mach disk. That is augmented gradually from 627 m/s at 3 NDL at 5 MPa (Fig. 3(a)) to 674 m/s at 5 NDL at 8 MPa (Fig. 3(d)). The Mach disks and stagnation points in the second recirculation zones locate downstream successively at each gas pressure (red arrows). Herein, the boundaries of the second recirculation zone are two stagnation points, and the length of this zone is much larger at 6 MPa than those at other gas pressures. After passing the second recirculation zone, the velocity profiles cross the zero velocity axis (green arrows) again at about 7 NDL, indicating the emergence of the third circulation zone, only when gas pressure is as high as 7 or 8 MPa. The length of this zone is longer at 8 MPa than that at 7 MPa. After passing this recirculation zone, the gas focuses its flow and oscillates at a velocity of 350 m/s until leaving the simulation domain.

Fig. 4 reveals the static pressure curves along the centerline of atomizer at each gas modeling pressure. A sub-ambient pressure appears before the stagnation front in primary recirculation zone. In a very short length, the static pressure sharply increases, reaching the maximum pressure at the stagnation front at about 1 NDL. At pressures ranging from 5 to 8 MPa, they are 613, 665, 863, and 968 kPa (blue arrows), respectively. Downstream of the stagnation

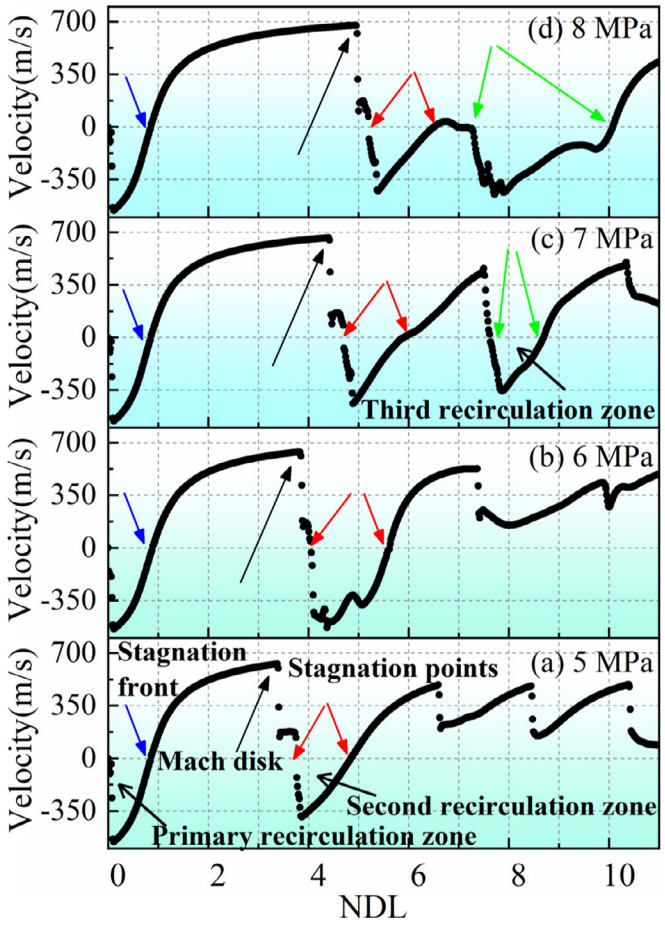

Fig. 3. The velocity profiles along the geometric centerline of the gas atomization nozzle at gas atomization pressures ranging from 5 to 8 MPa. The blue arrow points to the stagnation front in the primary recirculation zone, the black arrow points to the Mach disk, the red arrows point to the stagnation points in the second recirculation zone, and the green arrows point to the stagnation points in the third recirculation zone.

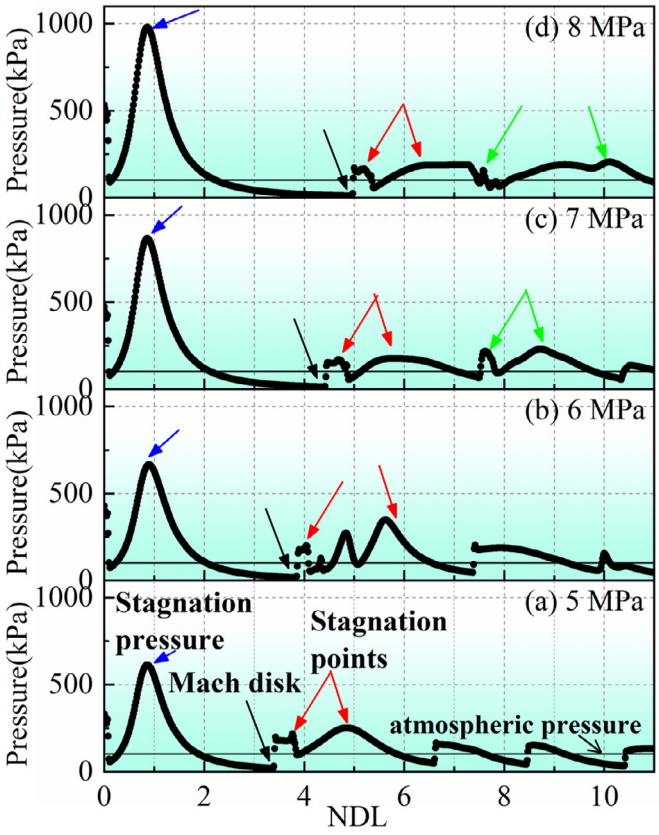

Fig. 4. The static pressure profiles along the geometric centerline of the gas atomization nozzle at gas atomization pressures ranging from 5 to 8 MPa. The blue arrow points to the stagnation front in the primary recirculation zone, the black arrow points to the Mach disk, the red arrows point to the stagnation points in the second recirculation zone, and the green arrows point to the stagnation points in the third recirculation zone.

fronts, the pressures fall sharply. Afterwards, the pressure drops gradually along the centerline until arriving at the Mach disk. After the Mach disk, the pressure curve reaches two minor static peaks (red arrows) at the stagnation points of the second recirculation zone. After crossing this zone, the static pressure curves oscillate around atmospheric pressure at 5 and 6 MPa (Fig. 4(a) and (b)). While, at higher gas pressures of 7 and 8 MPa (Fig. 4(c) and (d)), after the second recirculation zone, two other minor static peaks (green arrows) appear downstream. Further, the static pressure is found to oscillate at 7 MPa, but the subsequent Prandtl-Meyer wave is not observed at 8 MPa, due to the limit of computational domain.

4.2. Simulation of gas-melt field

Fig. 5 depicts temporal evolution of the gas-melt flow at 8 MPa gas pressure. Firstly, injected into the atomization chamber through the melt orifice (Fig. 5(a)), the liquid melt encounters the upstream gas in the primary recirculation zone and spreads laterally close to the orifice. Later, it is squeezed to a thin circular sheet (Fig. 5(b)). At 30 μs, the initial break-up of the melt sheet occurs at the edge of the orifice tip, due to the impingement of the high-speed gas stream (Fig. 5(c)). Then the liquid droplets flow with the gas to the centerline (Fig. 5(d)). At 50 μs, the large melt droplets collide and coalesce at the centerline (Fig. 5(e)), and flow downstream along the centerline at 60 μs as shown in Fig. 5(f) and at 100 μs in Fig. 5(g).

Some apparent variations of CFD model of the gas atomization nozzle appear after taking the melt droplets into consideration. Fig. 6 elucidates the velocity field in the gas-melt flow condition. At 5 MPa (Fig. 6(a)), the size of the primary recirculation zone is reduced due to the low-speed and incompressible features of droplets. Beyond this zone, the droplets traverse the intermediate intersection of the gas flow, forming a triangle-shaped high-speed shock pattern at the centerline. Then, they impact upon the Mach disk, forming "*S*"-shaped Mach disk. When the modeled pressure reaches 6 and 7 MPa (Fig. 6(b) and (c)), the Mach disks extend downstream, turning into "*Z*"-shape. Meanwhile, the second recirculation zones are elongated. At an atomization pressure of 8 MPa, the triangle-shaped shock is up to the maximum both in width and length. The second recirculation zone downstream is divided into two portions along the centerline. At this time, the vortexes are located on both sides of the central axis (Fig. 6(d)).

Fig. 7 demonstrates the velocity profiles along the axis of symmetry of gas-melt flow field at each gas modeling pressure. These profiles manifest different amounts of velocity loss under different gas pressures. Upstream locations of stagnation fronts are indicated by blue arrows. After the stagnation front, the gas stream speeds up along the axis to the maximum. Apparently, there are steep down gradients occurring during the acceleration. In addition, the Mach disk and stagnation point in the second recirculation zone (red arrows) extend downstream successively. Meanwhile, the length of the second recirculation zone is enlarged when

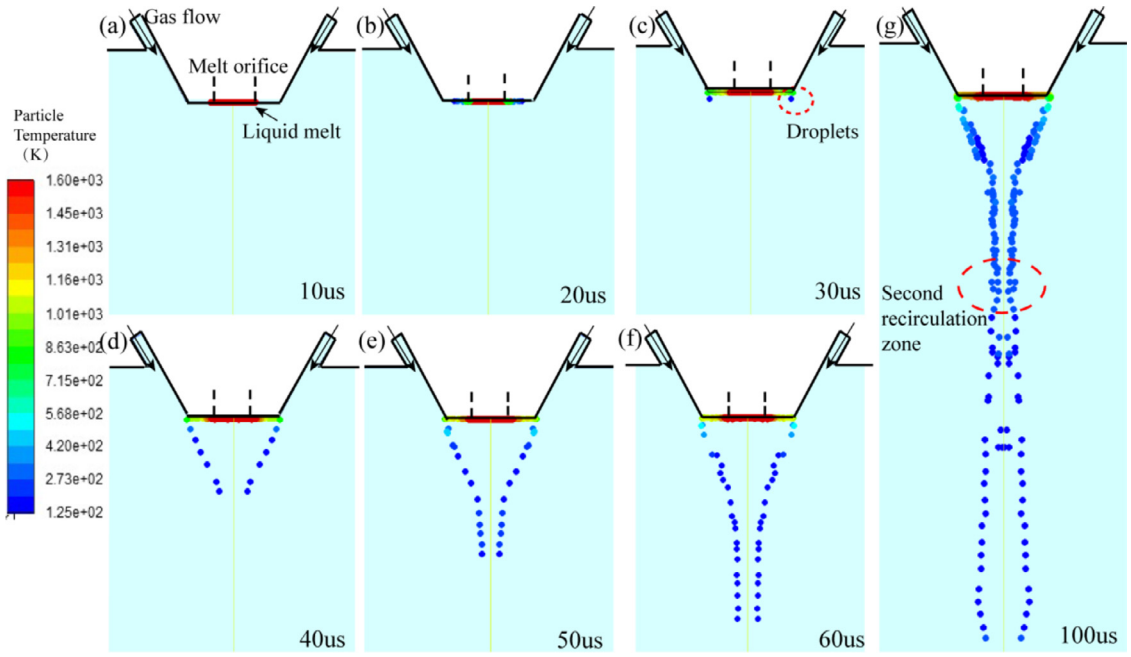

Fig. 5. Temporal evolution of the gas-melt flow at 8 MPa gas pressure. (a) A little melt at the orifice; (b) a thin circular sheet at the bottom of the melt delivery tube; (c) the initial break-up of the melt sheet at the edge of the tube; (d) the flowing liquid droplets to the centerline; (e) collision at the centerline; (f) flowing downstream along the centerline; (g) fine droplets after the second recirculation zone.

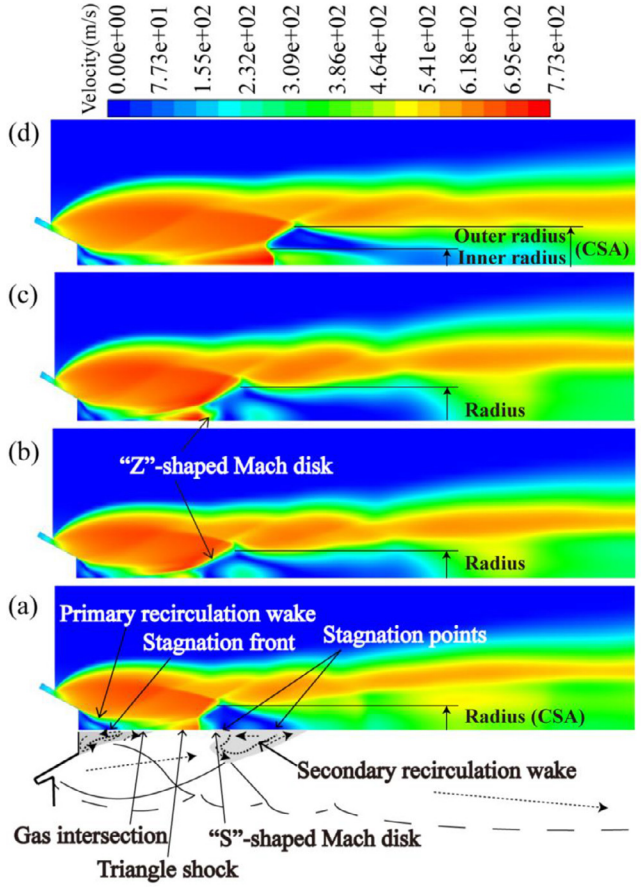

Fig. 6. CFD model of the gas atomization nozzle at gas atomization pressures ranging from 5 to 8 MPa in the closed-wake condition with multiple phase flows (gas and melt). The velocity magnitude increases - shades of darkness decreases. (a) "*S*"-shaped Mach disk; (b) "*Z*"-shaped Mach disk; (c) "*Z*"-shaped Mach disk; (d) vortex off the central line.

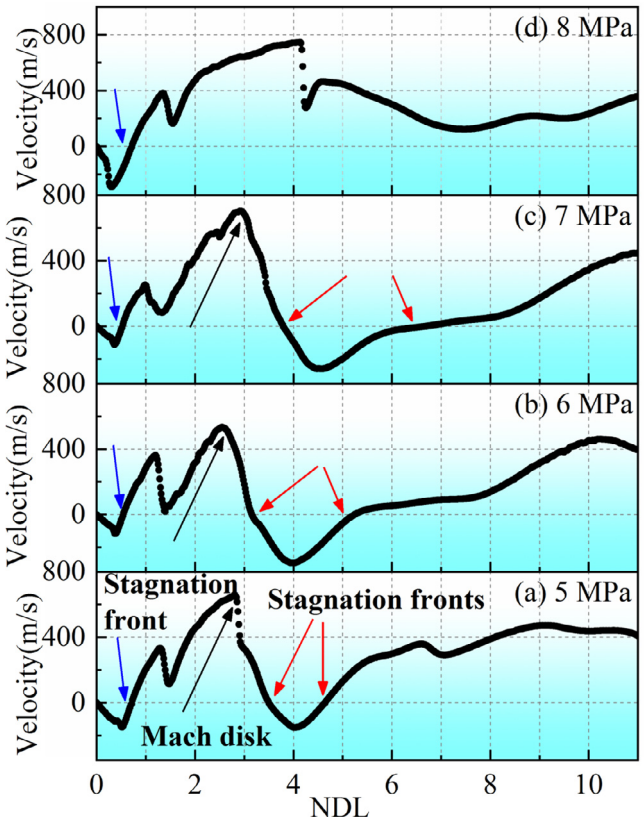

Fig. 7. The velocity profiles along the geometric centerline of the gas atomization nozzle respectively at gas atomization pressures ranging from 5 to 8 MPa with multiple phase flows (gas and melt). The blue arrow points to the stagnation front in the primary recirculation zone, the black arrow points to the mach disk, and the red arrows point to the stagnation points in the second recirculation zone.

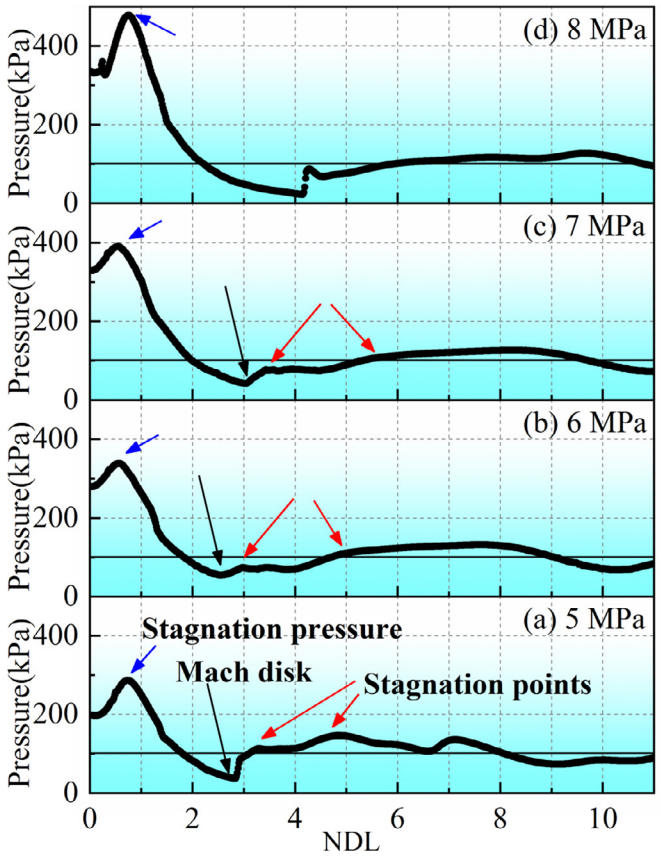

Fig. 8. The static pressure profiles along the geometric centerline of the gas atomization nozzle, respectively at gas atomization pressures ranging from 5 to 8 MPa with multiple phase flows (gas and melt). The blue arrow points to the stagnation front in the primary recirculation zone, the black arrow points to the Mach disk, and the red arrows point to the stagnation points in the second recirculation zone.

the gas pressure raises from 5 MPa to 7 MPa. However, at 8 MPa, the second recirculation zone is off the central line.

The static pressure curves along the axis of the atomizer at each gas modeling pressure are shown in Fig. 8. At the melt orifice position, the static pressure increases from 200 to 350 kPa as the gas pressure increases from 5 to 8 MPa. On the stagnation fronts in primary recirculation zones, the static pressures reach the maximum at 0.8 NDL. At gas pressures ranging from 5 to 8 MPa, they are 287, 338, 390, and 477 kPa (blue arrows), respectively. Beyond these maximum points, the pressures decrease steeply along the centerline, and the Mach disks are established subsequently. Beyond the Mach disks, two minor static pressure peaks (red arrows) are encountered at the stagnation points of the second recirculation zones ranging from 5 to 7 MPa. Meanwhile, the lengths between two minor static peaks are increased. However, at 8 MPa, the minor static peak is off the central line (Fig. 8(d)). Beyond this zone, the pressures float above and below the atmospheric pressure irregularly in the computational domain.

Fig. 9 shows the complicated geometric and velocity distribution of droplets at the modeled pressure of 8 MPa. Obviously, the droplets undergo a sectionalized fragmentation process with rapid reduction of their sizes. There are apparent changes in the diameters of droplets during atomization in three regions. At the edge of the orifice tip, the droplets start to form and accelerate (Inset A). And the molten alloy particles converge at the gas stream intersection position, moving downstream with lower velocities (Inset B). Afterwards, the droplets are disintegrated into fine particles as a result of high velocity gas flow (Inset C).

Table 2
Comparison and relative errors of the mean values (μ_G) and standard deviations (σ_G) of experimental and simulated frequency density distribution.

Pressure (MPa)		Experiment (μm)	Simulation (μm)	Error (%)
5	μ_G	78.47 ± 1.02	76.52 ± 1.22	2.49
	σ_G	60.56 ± 2.02	64.80 ± 2.55	7.03
6	μ_G	60.30 ± 0.58	62.14 ± 0.51	3.05
	σ_G	41.10 ± 1.15	44.21 ± 1.26	7.57
7	μ_G	52.86 ± 0.48	56.02 ± 1.11	5.79
	σ_G	33.07 ± 0.94	34.41 ± 2.55	4.05
8	μ_G	39.91 ± 0.28	36.79 ± 0.45	7.82
	σ_G	25.23 ± 0.55	28.48 ± 0.99	9.23

Plotted in the form of frequency curves at diameter scales, Fig. 10 demonstrates the simulation results of Fe-based alloy powder. It exhibits a good log-normal size distribution at each pressure. It is observed that, with the increment of gas pressure, the centroid of the particle size distributions move left and tend to be narrower, indicating that the diameter of powders becomes smaller and more concentrated.

4.3. Verification

Mathematical information of the frequency density distribution in experimentally-generated atomization is essential to assess the performance of atomizers. Fig. 10 compares the experimental and simulation values of the frequency density distribution. The experimental and simulation results fit well and the detailed information about the mean values (μ_G) and standard deviations (σ_G) of powder particle sizes are given in Table 2. As shown, μ_G of particles decreases with increasing gas atomizing pressure, suggesting a favorable part on the refinement of the powder with gas atomization pressure. In addition, σ_G tends to be reduced with the increase of atomization pressure, implying that the particle size distribution of powders becomes more concentrated as the gas pressure is increased. The errors between the simulation values and the experimental data are always less than 10%.

After sieving through a vibrating screen, we obtain the amorphous powders with diameters in the range of 25–45 μm in different gas atomization pressures. Fig. 11 illustrates SEM images of these Fe-based amorphous alloy powders at pressures of 5 to 8 MPa. On the whole, the powders are spherical and smooth, while there are a small number of short bar, spindle shape particles and very limited aggregated powders due to the occurrence of insufficient droplet-broken process. Fig. 12 demonstrates the diffraction patterns of Fe-based alloy powders with diameters of 25–45 μm atomized at pressures of 5 to 8 MPa. They display broad halo peaks without any apparent crystalline peak, implying their fully amorphous structure.

5. Discussion

5.1. Feature and transition of gas flow field

Recently, much effort has been devoted to explore the transition of “open-wake” and “closed-wake” and its major effect of gas atomization [20,30]. This was investigated by Ting and Anderson [20], who showed that, in the closed-wake condition, a “bowed” Mach disk structure and a second recirculation zone were formed at a gas pressure of 4.82 MPa. Although the physical behavior during the production of MG powders in the closed-wake condition has been clearly elucidated up to date, their physical process after the “closed-wake” condition remains mysterious. Thus, in this study, at 5 MPa (Fig. 3(a)), an augmented gas pressure after the “closed-wake” condition, illustrating a Mach disk structure and a

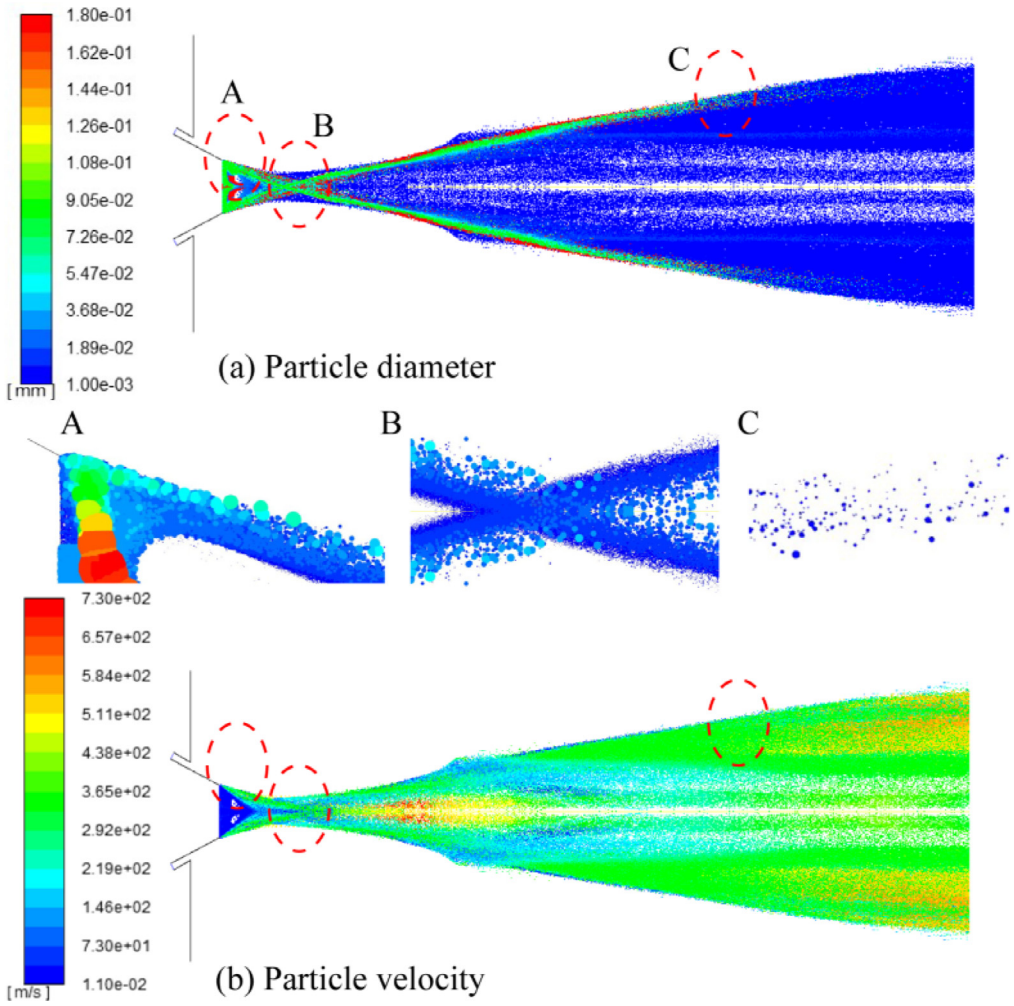

Fig. 9. The particle diameter (a) and the particle velocity (b) in the gas atomization process simulated via the WAVE model at gas atomization pressure of 8 MPa. Region A: the forming and accelerating droplets. Region B: the converging of droplets in the centerline with lower velocities. Region C: the second break-up process.

second recirculation zone. However, unlike the uniform second recirculation zone reported in the previous simulated image [20], the second recirculation zone simulated in this study provides more detailed information. As demonstrated in Fig. 13, the gas decelerates downstream at a steep gradient in one part, while it flows upstream and accelerates in the other. A vortex shows a varying deceleration condition. Such a condition arises from the fact that the gas velocity, crossing the "bowed" Mach disk surface, is likely to be non-uniform and unbalanced [20]. After passing this Mach disk, the gas stream flows straight along the axis, but the velocity vectors far away from the axis immediately acquire radial velocity components. Therefore, this uneven deceleration causes the gas vortex.

At 6 MPa, the shape of the second recirculation zone is elongated and transforms into an hourglass shape, in Fig. 3(b). At a gas pressure of 7 MPa (Fig. 3(c)), the third recirculation zone appears, elucidating the second Mach disk structure. When the gas pressure is 8 MPa, an enlarged third recirculation zone appears. It should be noted that, (1) with the increase of gas pressure, the primary recirculation zones alter little after the "closed-wake" pressure, even if the second recirculation zones are enlarged, and the third recirculation zones appear; (2) the second recirculation zones remain stable when the third recirculation zone appears. These two phenomena indicated, in gas flow field, only the last recirculation zone is affected by the retarded gas pressure, which is consistent with a previous report [13]. One explanation is that the Mach disk plays as a barrier and stops any upstream gas flow towards the recirculation zone [31]. Moreover, the stagnation pressures in the primary recirculation zones are almost one order of magnitude larger than others in the second and third zones. This damping is mainly due to ambient friction [32]. These high pressures provide supports for the existence of high stability of the recirculation zones before.

5.2. Droplet break-up process

It is realized that the break-up process of the melt can be divided into two portions: the primary and the second break-up. The melt is disrupted into large droplets during the primary break-up, and then divided into small ones during the second break-up. The entire process is shown in Fig. 14(a).

The primary break-up is given in Fig. 14(b–e). In the beginning, the molten alloy is poured into the chamber through the melt tube (Fig. 14(b)). Influenced by the gas flow from the forward direction in the primary recirculation zone (Fig. 14(c)), the molten alloy begins to spread and forms a thin sheet under the bottom of the melt pour tube (Fig. 14(d)). Afterwards, the molten alloy is impacted by the high-speed gas at the edge of the orifice tip, generating large droplets (Fig. 14(e)). The simulated primary break-up in our work is observed in Fig. 5. This prefilming operation was firstly presented by Unal, who took pictures using high-speed flash photography [33]. But the upturned orifice they used supplied a relatively low-speed gas flow. An approximate simulation result was

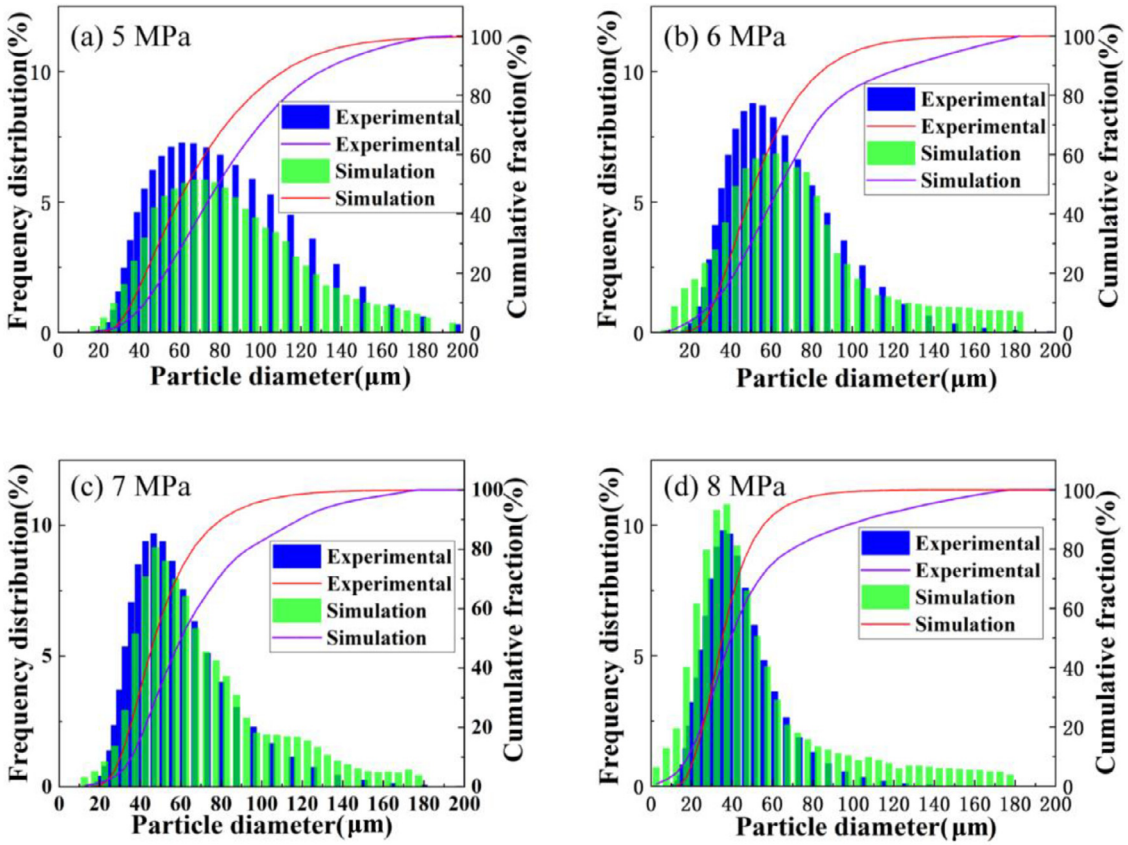

Fig. 10. The frequency density distribution obtained via the atomization simulation and actual gas atomization technology: (a) 5, (b) 6, (c) 7, (d) 8 MPa.

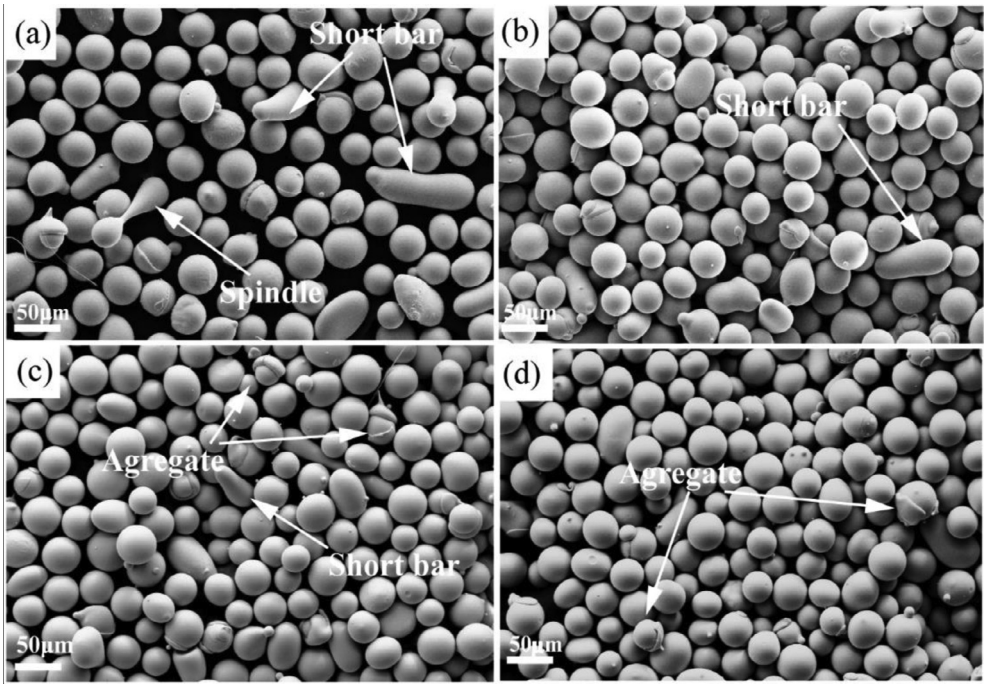

Fig. 11. SEM images of Fe-based amorphous powders ranging from 25 to 45 μm. (a) 5; (b) 6; (c) 7; (d) 8 MPa.

made in Ref. [34], and the melt moved upwards due to strong gas recirculation. Contrary to this study, they injected the melt into the chamber before the gas. Thus, the melt stream was penetrated by the following gas steam at the beginning of the disintegration. And the experiment result confirmed this phenomenon in Ref. [34]. In our work, the alloy frozen at the nozzle has a hollow cone in the center, which was formed during the atomization experiment, consistent with the simulation of the primary disintegration. Some droplets rotate in the primary recirculation zone, while the others fly downwards with the gas stream. Consequently, the new recirculation zone now in the gas-melt flow field is smaller in size as well as weaker in strength than the gas flow condition (Figs. 3 and

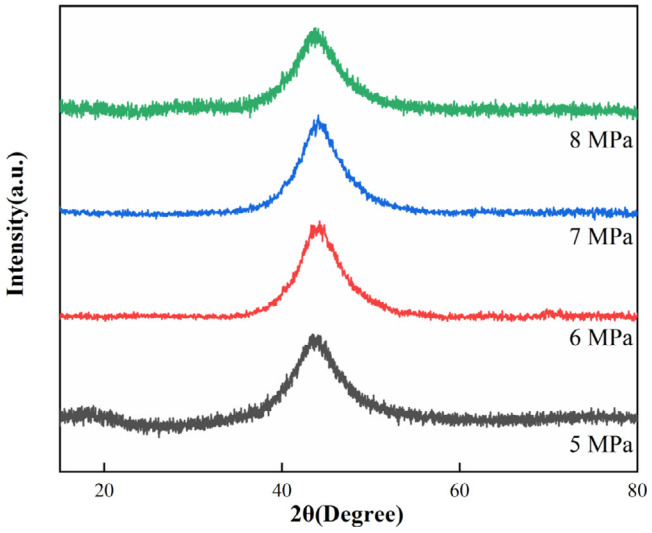

Fig. 12. XRD patterns of the Fe-based amorphous powders ranging from 25 to 45 μm at gas atomization pressures ranging from 5 to 8 MPa.

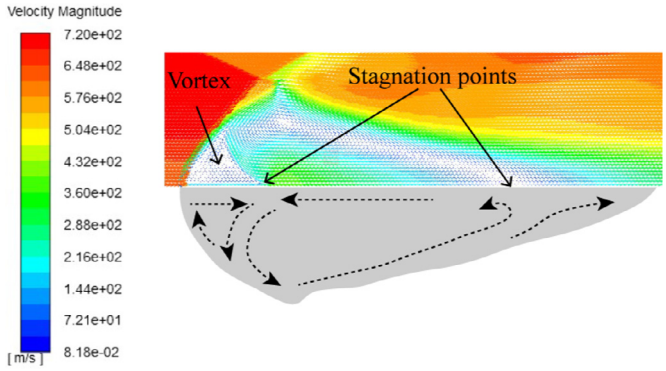

Fig. 13. Partial velocity vector and the mirroring schematics of the gas flow structures in the second recirculation zone at 5 MPa. Left-vortex downstream; right-vortex upstream.

7). A similar phenomenon has been reported in Wei et al.'s paper [24].

Intriguingly, before the second break-up process, the large droplets collide with each other at the centerline (Fig. 14(f)), resulting in a decreased velocity. Then, under the impact of gas flow with high speed, the large droplets are disrupted and accelerated, until encountering the second recirculation zone. In this zone, the droplets are forced to slow down, and disintegrate further outside this zone due to the impingement of the high-speed gas. It is worth noting that, the droplets, crossing the second recirculation zone, are able to get further break-up as a result of the larger relative speed between the gas flow and the melt particles (Fig. 14(g)). So, we potentially propose a factor, *i.e.*, the cross section area (CSA) of the second recirculation zone (marked in Fig. 6). It is in proportion to the number of droplets through it, herein, it can be used to reflect the extent of melt fragmentation. The CSAs are 40.47 mm^2, 53.04 mm^2, 76.32 mm^2 and 83.48 mm^2, respectively. It is found that the CSA increases with the increase of gas pressure, resulting in finer powders. This indicates that a higher pressure tends to a lower CSA, deriving from the increased inner radius and the constant outer radius.

Meanwhile, the relatively large droplets spread more widely and dominate the outer part of the atomization region. This phenomenon could be ascribed to that, under the shear force, in the peripheral region, the smaller droplets tend to move close to the axis, while the bigger ones incline to be entrained to the peripheral domain [35]. Another explanation is that the middle part of the spray has a larger velocity and greater turbulence than those at the 'outside', therefore, it can enhance the atomization disintegration and secondary droplets appear within the center region. The decreasing particle size towards the centerline of atomization is also observed in the simulated and experimental data of Jing et al.'s essay [35].

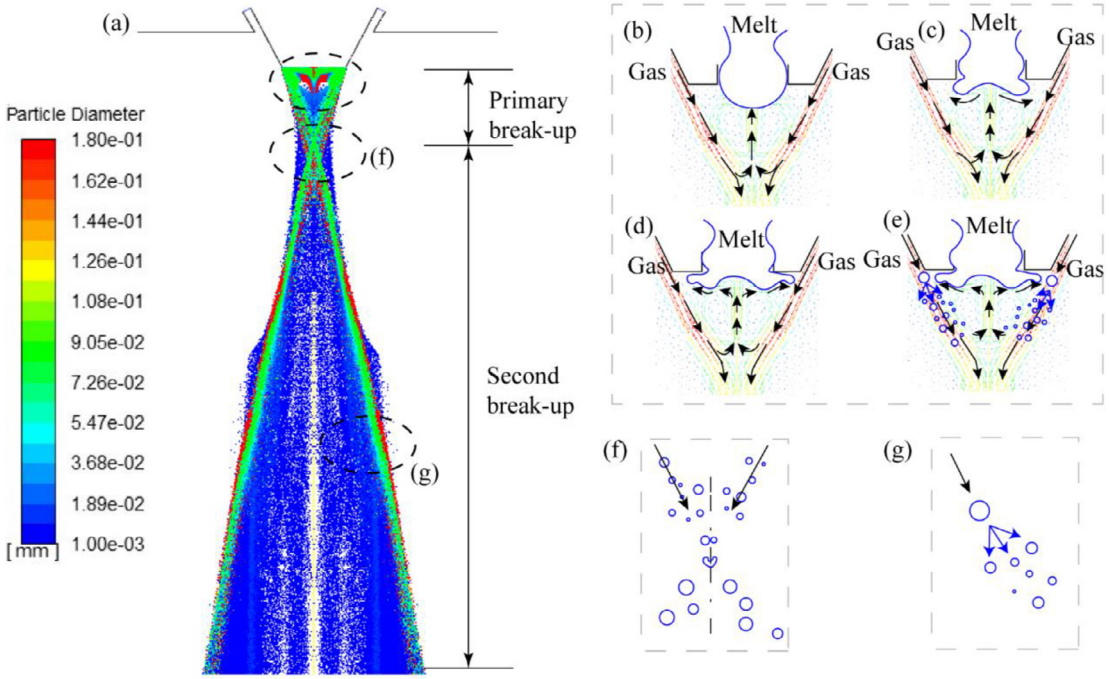

Fig. 14. (a) The droplet break-up process. (b) The injection of melt into the chamber; (c) the deformed melt under the upstream gas; (d) a thin sheet of the melt; (e) forming the large droplets; (f) the collision at the centerline; (g) the second break-up.

6. Conclusions

Simulation of the gas atomization process for Fe-based amorphous alloy powder production ranging from 5 to 8 MPa was conducted by employing the numerical method that was the combination of Realizable k-ε mode and DPM theory. This study illustrated the anatomical gas profiles of gas flow and gas-melt flow fields, and analyzed the break-up process. Besides, the particle size distributions were predicted, and compared with the experimental results. The main findings can be summarized as follows.

(1) In the gas flow field, at 5 MPa, the second recirculation zone appears under the exit, in the closed-wake condition. Then, the third recirculation zone appears at pressures above 7 MPa. The last recirculation zone is enlarged and truncated, while the others remain stable with the augmented pressures.
(2) In the gas-melt field, the primary recirculation zone has a smaller size and lower upstream velocity, compared to the gas flow field. Under the impact of the droplet flow of increasing gas pressure, the Mach disk changes from "bowed" shape to "*S*"-shape and "*Z*"-shape, and finally at 8 MPa, it is divided into two portions along the center. The second recirculation zone at 7 MPa is twice as large as that at 5 MPa. At 8 MPa, the divided zones are located on both sides of the central axis.
(3) The experimental results are consistent well with the simulations. In the primary breakup, the melt spreads and forms at the bottom of the melt delivery tube, and large droplets are generated at the edge of the tube. In the secondary breakup, the droplets, crossing the second recirculation zone, have relatively low velocities and can undergo further fragmentation.

Data availability

The experimental data from this study are available from Master Y.T. Shi (Email: ytshi17b@imr.ac.cn) of the University of Science and Technology of China upon reasonable request.

Declaration of Competing Interest

The authors declare that they have no known competing financial interests or personal relationships that could have appeared to influence the work reported in this paper.

CRediT authorship contribution statement

Yutong Shi: Methodology, Investigation, Writing – original draft, Writing – review & editing, Resources. **Weiyan Lu:** Methodology, Data curation. **Wenhai Sun:** Methodology, Data curation. **Suode Zhang:** Methodology, Data curation, Resources. **Baijun Yang:** Data curation. **Jianqiang Wang:** Conceptualization, Methodology, Writing – original draft, Writing – review & editing, Resources, Project administration.

Acknowledgments

This work was supported by the National Key Research and Development Program of China (No. 2016YFB1100204), the Key Research & Development Plan of Jiangxi Province (No. 20192ACB80001), and the National Natural Science Foundation of China (Nos. 52171163, 51701214 and U1908219). The authors were also grateful to C.J. Wang, from Aero Engine Corporation of China, and Y.P. Wang, from The University of New South Wales, Australia, for fruitful discussions.

References

[1] H. Qi, M. Azer, A. Ritter, Metall. Mater. Trans. A 40 (2009) 2410–2422.
[2] W.J. Sames, F.A. List, S. Pannala, R.R. Dehoff, S.S. Babu, Int. Mater. Rev. 61 (2016) 315–360.
[3] D. Herzog, V. Seyda, E. Wycisk, C. Emmelmann, Acta Mater. 117 (2016) 371–392.
[4] J.A. Slotwinski, E.J. Garboczi, P.E. Stutzman, C.F. Ferraris, S.S. Watson, M.A. Peltz, J. Res. Natl. Inst. Stand. Technol. 119 (2014) 460–493.
[5] J. Trapp, A.M. Rubenchik, G. Guss, M.J. Matthews, Appl. Mater. Today 9 (2017) 341–349.
[6] J.H. Martin, B.D. Yahata, J.M. Hundley, J.A. Mayer, T.A. Schaedler, T.M. Pollock, Nature 549 (2017) 365–369.
[7] Y. Lu, H. Zhang, H. Li, H. Xu, G. Huang, Z. Qin, X. Lu, J. Non Cryst. Solids 461 (2017) 12–17.
[8] T. DebRoy, H.L. Wei, J.S. Zuback, T. Mukherjee, J.W. Elmer, J.O. Milewski, A.M. Beese, A. Wilson-Heid, A. De, W. Zhang, Prog. Mater Sci. 92 (2018) 112–224.
[9] I. Todd, Nature 549 (2017) 342–343.
[10] X. Zhao, J. Chen, X. Lin, W. Huang, Mater. Sci. Eng. A 478 (2008) 119–124.
[11] D.D. Gu, W. Meiners, K. Wissenbach, R. Poprawe, Int. Mater. Rev. 57 (2013) 133–164.
[12] N. Zeoli, S. Gu, Comput. Mater. Sci. 38 (2006) 282–292.
[13] F.S. Biancaniello, P.I. Espina, G.E. Mattingly, S.D. Ridder, Mater. Sci. Eng. 119 (1989) 161–168.
[14] T. Fedina, J. Sundqvist, J. Powell, A.F.H. Kaplan, Addit. Manuf. 36 (2020) 1–11.
[15] D. Beckers, N. Ellendt, U. Fritsching, V. Uhlenwinkel, Adv. Powder Technol. 31 (2020) 300–311.
[16] N. Zeoli, S. Gu, Comput. Mater. Sci. 42 (2008) 245–258.
[17] Y. Shen, Y. Li, C. Chen, H.L. Tsai, Mater. Des. 117 (2017) 213–222.
[18] N. Ciftci, Cooling Strategies for the Atomization of Glass-Forming Alloys, Universität Bremen, 2020 Ph.D. Thesis.
[19] J. Ting, M.W. Peretti, W.B. Eisen, Mater. Sci. Eng. A 326 (2002) 110–121.
[20] J. Ting, I.E. Anderson, Mater. Sci. Eng. A 379 (2004) 264–276.
[21] N. Zeoli, S. Gu, Comput. Mater. Sci. 43 (2008) 268–278.
[22] X.G. Li, U. Fritsching, J. Mater. Process. Technol. 239 (2017) 1–17.
[23] J.S. Thompson, O. Hassan, S.A. Rolland, J. Sienz, Powder Technol. 291 (2016) 75–85.
[24] M. Wei, S. Chen, M. Sun, J. Liang, C. Liu, M. Wang, Powder Technol. 367 (2020) 724–739.
[25] S. Jeon, M.P. Sansoucie, D.M. Matson, J. Chem. Thermodyn. 138 (2019) 51–58.
[26] H.X. Li, Z.C. Lu, S.L. Wang, Y. Wu, Z.P. Lu, Prog. Mater. Sci. 103 (2019) 235–318.
[27] Y. Li, W.Z. Chen, B.S. Dong, S.X. Zhou, J. Non Cryst. Solids 496 (2018) 13–17.
[28] P.J. O'Rourke, A.A. Amsde, in: Proceedings of the International Fuels and Lubricants Meeting and Exposition, Toronto, Ontaio, 1987 November 2-5.
[29] R.D. Reitz, Mechanisms of atomization processes in high-pressure vaporizing sprays, At. Spray Technol. 3 (1987) 309–337.
[30] M. Wei, S. Chen, J. Liang, C. Liu, Vacuum 143 (2017) 185–194.
[31] J. Ting, U. Habel, M.W. Peretti, W.B. Eisen, R. Young, B. Chao, B. Huang, Mater. Sci. Eng. A 329-331 (2002) 372–376.
[32] M.R. Ridolfi, P. Folgarait, Int. J. Multiph. Flow 132 (2020) 103431.
[33] A. Unal, Mater. Sci. Technol. 3 (1987) 1029–1039.
[34] K. Hanthanan Arachchilage, M. Haghshenas, S. Park, L. Zhou, Y. Sohn, B. McWilliams, K. Cho, R. Kumar, Adv. Powder Technol. 30 (2019) 2726–2732.
[35] D. Jing, F. Zhang, Y. Li, H. Xu, S. Shuai, Fuel 199 (2017) 478–487.